



# The role of submerged berms on the momentary liquefaction around conventional rubble mound breakwaters

Daniele Celli<sup>a,c,\*</sup>, Yuzhu Li<sup>b</sup>, Muk Chen Ong<sup>b</sup>, Marcello Di Risio<sup>c</sup>

<sup>a</sup> Department of Civil, Environmental, Territory, Building and Chemical Engineering, Technical University of Bari, Bari, Italy

<sup>b</sup> Department of Mechanical and Structural Engineering and Materials Science, University of Stavanger, Stavanger, Norway

<sup>c</sup> Department of Civil, Construction-Architectural and Environmental Engineering, University of L'Aquila, L'Aquila, Italy

## ARTICLE INFO

### Keywords:

Breakwaters

Berm

SWASH

Momentary liquefaction

Numerical models

## ABSTRACT

Berms deployed at the toe of conventional rubble mound breakwaters can be very effective in improving the stability of the armor layer. Indeed, their design is commonly tackled by paying attention to armor elements dimensioning. Past research studies showed how submerged berms can increase the stability of the armor layer if compared to straight sloped conventional breakwaters without a berm. To fill the gap of knowledge related to the interaction between breakwaters with submerged berm, waves and soil, this research aims to evaluate how submerged berms configuration influences the seabed soil response and momentary liquefaction occurrences around and beneath breakwaters foundation, under dynamic wave loading. The effects of submerged berms on the incident waves transformation have been evaluated by means of a phase resolving numerical model for simulating non-hydrostatic, free-surface, rotational flows. The soil response to wave-induced seabed pressures has been evaluated by using an ad-hoc anisotropic poro-elastic soil solver. Once the evaluation of the seabed consolidation state due to the presence of the breakwater has been performed, the dynamic interaction among water waves, soil and structure has been analyzed by using a one-way coupling boundary condition. A parametric study has been carried out by varying the berm configuration (i.e. its height and its length), keeping constant the offshore regular wave condition, the berm and armor layer porosity values, the water depth and the elastic properties of the soil. Results indicate that the presence of submerged berms tends to mitigate the liquefaction probability if compared to straight sloped conventional breakwater without a berm. In addition, it appears that the momentary liquefaction phenomena are more influenced by changing the berm length rather than the berm height.

## 1. Introduction

Conventional rubble mound breakwaters are widely used all over the world, mainly to provide protection for harbors (e.g. Van Der Meer [40]) and to preserve coastal areas (e.g. Lamberti et al. [19], Di Risio et al. [8], Saponieri et al. [30]) from currents and wave actions. Therefore, the design of the breakwaters is aimed to ensure stability against such environmental loads. Furthermore, in order to limit the scour induced by the coastal currents (e.g. Saponieri et al. [29]) and the storm surge (e.g. Pasquali et al. [28]), and to increase the stability of the armor layer (e.g. Celli et al. [5], Van Gent [41]), it can be appropriate to modify the straight slopes of conventional breakwaters, by deploying a submerged berm marked by a higher length than usual. As reported in literature (e.g. Franco [11], Oumeraci [27], Chung et al. [6], Elsafti and Oumeraci [9,10], Zhao et al. [46]), some of the failures

experienced by coastal structures are likely due to geotechnical causes, such as the wave-induced liquefaction. It could be hence interesting to evaluate the performance of submerged berms of reducing the liquefaction probability in the soil, in the vicinity of the breakwaters.

When water waves propagate over a non-cohesive seabed and interact with coastal structures, excess pore pressure can be generated, enabling the rise of two different types of liquefaction (Nago et al. [25]): the “residual” liquefaction and the “momentary” liquefaction. The “residual” liquefaction is caused by compression-relaxation cycles under wave crests and wave troughs, respectively. It generates shear stresses in the soil and the consequent buildup of pore water pressure that could exceed the value of the overburden pressure, making the soil grains totally unbound (Sumer [33]). The “momentary” liquefaction occurs during the passage of wave troughs if the upward pore pressure gradient (strictly related to seepage forces) exceeds the initial vertical

\* Corresponding author at: Department of Civil, Environmental, Territory, Building and Chemical Engineering, Technical University of Bari, Bari, Italy.

E-mail address: [daniele.celli@poliba.com](mailto:daniele.celli@poliba.com) (D. Celli).

effective stress. When a pore pressure gradient exists, a seepage flow arises (e.g. Zen and Yamazaki [45]). It generates seepage forces on the soil skeleton in the direction of the flow, as seen from Figures 13 and 14 in Ye et al. [44]. At the passage of wave crests are hence associated seepage forces acting downwards, enhancing the grain compaction, excluding liquefaction occurrences. On the contrary, upward seepage forces, generated under the wave troughs, may uplift the soil, inducing seabed instability (Jeng and Ye [15]).

The work proposed herein deals with rubble mound breakwaters with submerged berms. The potential structure failure of rubble mound breakwaters may result from both residual and transient pore pressure generation. The present work is focused on the evaluation of submerged berms configuration only upon momentary liquefaction occurrences.

In the past decades, research studies have been carried out on the interaction between waves, seabed and structures (hereinafter referred to as WSSI). In this regard, Mase et al. [24] and Hur et al. [13] used the classic Biot's poro-elastic theory to investigate the seabed response around a composite caisson-type breakwater by using numerical tools. Ulker et al. [37], Ye et al. [44,42] and Zhao et al. [46] simulated the presence of a composite caisson-type breakwater in their numerical models, showing that the assessment of the consolidation process, in presence of marine structures, is essential for the liquefaction analysis. In particular, Ulker et al. [37] studied the instability of the porous seabed-rubble foundation due to the momentary liquefaction, by adopting three different formulations for the Biot's equations. Ye et al. [44] investigated the interaction between breaking waves, seabed foundation and composite breakwater, by carrying out a parametric study about the maximum momentary liquefaction depth as a function of the soil properties and the wave characteristics. Furthermore, Ye et al. [42] and Zhao et al. [46] focused their attention on the residual liquefaction around the structure, under the combined action of both waves and caisson rocking motions. To remain within the breakwater framework, Zhao and Jeng [48] carried out a parametric study on the effects of wave and soil characteristics, as well as bed slopes, on the wave-induced residual liquefaction in the vicinity of a breakwater. Liao et al. [21,22] used both a three-dimensional integrated numerical scheme to evaluate the WSSI around a slope-type breakwater head. Their results showed that the breakwater slope has significant effects on the seabed response. In particular, an increase of the breakwater slope could intensify the soil response and the liquefaction probability around the breakwater head. Zhao et al. [47] developed a numerical model to investigate the interactions between waves, currents, a submerged rubble mound breakwater and its poro-elastic seabed foundations. Their results showed the significant influences of currents on the local hydrodynamic process and the resulting dynamics of seabed foundation around a submerged rubble mound breakwater.

To date, the effects of submerged berms on the liquefaction phenomenon around rubble mound breakwaters have been given little attention in the literature. Therefore, the aim of the present research is to investigate the wave-induced soil response and momentary liquefaction probability around and beneath rubble mound breakwaters with submerged berm. A parametric study has been carried out by varying the berm configuration in terms of its length and its height, keeping constant the elastic properties of the soil, the berm and the armor layer porosity values, the water depth and the offshore regular wave condition. This is to assess if the introduction of a submerged berm will provide improvements in terms of reduction of liquefaction probability, if compared to the case of straight sloped conventional breakwaters without a berm. The adopted rationale, based on a parametric-comparative study, makes reasonable the regular wave assumption, despite irregular waves always occur in real ocean environments. The features of the present work are:

- (i) the water waves hydrodynamic properties have been evaluated by means of SWASH, an open source phase resolving numerical model for simulating non-hydrostatic, free-surface, rotational flows

(Zijlema et al. [50]), due to its efficiency;

- (ii) an open-source poro-elastic soil solver including both consolidation and liquefaction analysis has been adopted for the present study. The soil model was developed within the Finite Volume Method (hereinafter referred to as FVM)-based OpenFOAM framework by Li et al. [20] and was already employed for the detection of momentary liquefaction occurrences within the WSSI framework. It takes into account the anisotropy since most of the natural soils show some degree of anisotropy, i.e., having different elastic and hydraulic properties in different directions, according to Hsu and Jeng [12]. The interaction between the multiple physical phases has been implemented by using the seabed dynamic pressure as one-way coupling boundary condition for the poro-elastic anisotropic soil model;
- (iii) a parametric study has been carried out to investigate the efficiency of a berm in reducing the momentary liquefaction phenomena. The optimal berm configuration has been identified from the parametric study.

Since the parametric study has involved 62 numerical simulations, SWASH is used to calculate the hydrodynamic properties associated to wave propagation in presence of porous structure (e.g. Celli et al. [5]) in a fast way and with low computational cost (about 2 h of wall clock time adopting 16 cores and 58 MB of pressure data per simulation produced). The usage of this type of tool enables to carry out an extensive parametric study in a reasonable time window.

## 2. Mathematical models and the coupling algorithm

### 2.1. The wave numerical model

The numerical model SWASH has been used to compute the water wave hydrodynamic properties within the wave-structure interaction framework. It is an open source phase resolving numerical model for simulating non-hydrostatic, free surface, rotational flows (Zijlema et al. [50]). The model has been widely validated and used within several research studies, including the interaction among waves and both impermeable (e.g. Marmoush et al. [23], Suzuki et al. [34]) and porous structures (e.g. Alabart et al. [1], van den Bos [3,4], Celli et al. [5]). In the followings, only a synthetic description of the model is illustrated. For further details, the reader can refer to the model manual (The SWASH team [35]). The model solves the shallow water equations including a non-hydrostatic pressure term that can be derived from the incompressible Navier-Stokes equations and a module for porous flow on the basis of Forchheimer's formulations. The former relationships are included in the porous momentum equations by means of two extra dissipative terms,  $f_l$  (laminar) and  $f_t$  (turbulent), equal to:

$$f_l = \alpha_0 \frac{(1-n)^3}{n^2} \frac{\nu}{D_{n50}^2} \quad f_t = \beta_0 \frac{(1-n)}{n^3} \frac{1}{D_{n50}} \quad (1)$$

where  $\alpha_0$  and  $\beta_0$  are the Forchheimer's coefficients,  $n$  is the porosity and  $D_{n50}$  represents the nominal diameter.

In the research described herein, the numerical model has been employed by using three terrain-following layers in the vertical direction in the one-dimensional case. Then, the layer-integrated continuity equation for layer  $1 \leq k \leq K$  ( $K = 3$ ) reads as follows (Zijlema and Stelling [51]):

$$\frac{\partial h_k u_k}{\partial x} - u \frac{\partial z}{\partial x} \Big|_{z_{k-1/2}}^{z_{k+1/2}} + w_{k+1/2} - w_{k-1/2} = 0 \quad (2)$$

where  $x$  is the horizontal coordinate,  $h_k$  is the thickness of the layer  $k$ ,  $z$  is the elevation of the interface between two layers (being  $z_{k-1/2}$  the interface between the layer  $k-1$  and the layer  $k$  and  $z_{k+1/2}$  the interface between the layer  $k$  and the layer  $k+1$ ),  $u$  is the layer-integrated horizontal velocity,  $w_{k\pm 1/2}$  is the vertical velocity at the

interfaces between two layers.

The layer-integrated horizontal momentum equation reads as follows:

$$\frac{\partial h_k u_k}{\partial t} + \frac{\partial h_k u_k^2}{\partial x} + \bar{u}_{k+1/2}^z \omega_{k+1/2} - \bar{u}_{k-1/2}^z \omega_{k-1/2} + g h_k \frac{\partial \zeta}{\partial x} + \frac{\partial h_k \bar{q}_k^z}{\partial x} - q_{k+1/2} \frac{\partial \zeta_{k+1/2}}{\partial x} + q_{k-1/2} \frac{\partial \zeta_{k-1/2}}{\partial x} = 0 \quad (3)$$

where  $t$  is the elapsed time,  $\bar{u}_{k\pm 1/2}^z$  is the horizontal velocity estimated at the layer interfaces  $z_{k\pm 1/2}$ ,  $\omega_{k\pm 1/2}$  is the vertical velocity relative to layer interface  $z_{k\pm 1/2}$  (defined as the difference between the vertical velocity along the streamline and the vertical velocity along the interface),  $g$  is the gravitational acceleration,  $\zeta$  is the free surface elevation,  $q_{k\pm 1/2}$  is the non-hydrostatic pressure defined at the layer interfaces,  $\bar{q}_k^z$  is the arithmetic mean of the non-hydrostatic pressure at the layer interfaces  $z_{k\pm 1/2}$ .

The layer-integrated vertical momentum equation reads as follows:

$$\frac{\partial h_{k+1/2} w_{k+1/2}}{\partial t} + \frac{\partial h_{k+1/2} \bar{u}_{k+1/2}^z w_{k+1/2}}{\partial x} + \bar{w}_{k+1}^z \bar{\omega}_{k+1}^z - \bar{w}_k^z \bar{\omega}_k^z + 2 \bar{q}_k^z = 0 \quad (4)$$

where  $h_{k+1/2}$  is the arithmetic mean of the layer thicknesses  $h_k$  and  $h_{k+1}$ ,  $\bar{w}_{k(+1)}^z$  is the arithmetic mean of the vertical velocities at the layer interfaces  $z_{k(+1)\pm 1/2}$ ,  $\bar{\omega}_{k(+1)}^z$  is the arithmetic mean of the vertical velocities relative to the layer interface at the layer interfaces  $z_{k(+1)\pm 1/2}$ .

The details of numerical procedures and boundary conditions can be referred to Zijlema and Stelling [49,51] and Smit et al. [31].

## 2.2. The soil numerical model

Within the soil model framework, the following assumptions have been made (Li et al. [20]):

- (i) the seabed has constant thickness;
- (ii) the soil is almost fully saturated;
- (iii) the soil skeleton obeys Hooke's law (i.e. is characterized by elastic properties);
- (iv) the Young's modulus, the Poisson's ratio and the constant soil permeability are different in vertical and horizontal directions (i.e. anisotropic condition).

The classical Biot's consolidation equations (Biot [2]) are adopted to model the coupled soil behavior with the interaction between the solid skeleton and the pore fluid, considering the anisotropic soil characteristics. The soil domain is governed by the quasi-static momentum balance equation for soil mixture and the mass balance equation of the pore fluid based on Darcy's law.

Quasi-static momentum balance equation is presented in Eq. (5):

$$\nabla \cdot \left[ \mathbf{C} : \frac{1}{2} (\nabla \mathbf{U} + (\nabla \mathbf{U})^T) \right] - \nabla p = 0 \quad (5)$$

where  $\mathbf{U}$  is the soil (skeleton) displacement,  $p$  is the pore fluid pressure and  $\mathbf{C}$  is the elastic stiffness tensor. For anisotropic soil materials, the two dimensional (hereinafter referred to as 2D) orthotropic elastic stress-strain relation can be expressed in a  $3 \times 3$  matrix notation:

$$\boldsymbol{\sigma}' = \begin{pmatrix} \sigma'_{xx} \\ \sigma'_{zz} \\ \sigma'_{xz} \end{pmatrix} = \begin{bmatrix} A_{11} & A_{12} & 0 \\ A_{12} & A_{22} & 0 \\ 0 & 0 & A_{33} \end{bmatrix} \begin{pmatrix} \epsilon_{xx} \\ \epsilon_{zz} \\ \epsilon_{xz} \end{pmatrix} = \mathbf{C} : \boldsymbol{\epsilon} \quad (6)$$

where  $\boldsymbol{\sigma}'$  is the effective stress tensor. The 4 independent coefficients  $A_{ij}$  are calculated from Young's modulus  $E_i$ , Poisson's ratio  $\nu_{ij}$  and the shear modulus  $G_{ij}$  as follows:

$$\begin{aligned} A_{11} &= \frac{E_x}{1 - \nu_{xz}\nu_{zx}} \\ A_{22} &= \frac{E_z}{1 - \nu_{zx}\nu_{xz}} \\ A_{12} &= \frac{\nu_{xz}E_z}{1 - \nu_{zx}\nu_{xz}} \\ A_{33} &= G_{xz} \end{aligned} \quad (7)$$

The mass balance equation of the pore fluid reads as follows:

$$\frac{n}{K'} \frac{\partial p}{\partial t} = -\frac{1}{\gamma_w} \nabla \cdot (\mathbf{k} \cdot \nabla p) + \frac{\partial}{\partial t} (\nabla \cdot \mathbf{U}) \quad (8)$$

where  $n$  denotes the soil porosity,  $\gamma_w$  represents the specific weight of the water in the soil, and  $\mathbf{k}$  denotes the diagonal permeability tensor with values  $k_x$  and  $k_z$ . The bulk modulus of the compressible pore flow  $K'$  is approximated through the formulation proposed by Vafai and Tien [39]:

$$\frac{1}{K'} = \frac{1}{K_w} + \frac{1 - S_r}{p_a} \quad (9)$$

where  $S_r$  represents the degree of soil saturation,  $K_w$  denotes the bulk modulus of pure water ( $\approx 2$  GPa), and  $p_a = \rho_w g d$  is the absolute pore water pressure, being  $\rho_w$  the water density.

A description of the boundary conditions adopted to solve the governing equations are discussed in Section 4.

## 2.3. Boundary coupling algorithm

The coupling procedure requires the information exchange in terms of dynamic wave pressure between the different domains involved in the WSSI, via the common boundary. Similar approach was adopted by Ye et al. [42] (see their Figure 1) within the FSSI-CAS 2D model. Then, two physical domains are selected: the first one is addressed to the interaction between waves and porous structures, whilst the second one is dedicated to the seabed response to the waves loads. The sheared boundary is at the seabed surface. The minor motion of the seabed soil does not alter the wave-porous structure domain, as depicted in Fig. 1. The dynamic wave pressure  $p_d$ , computed at the seabed layer and beneath the porous structure, transfers to the soil domain as a dynamic boundary condition. In the model, time-varying boundary conditions

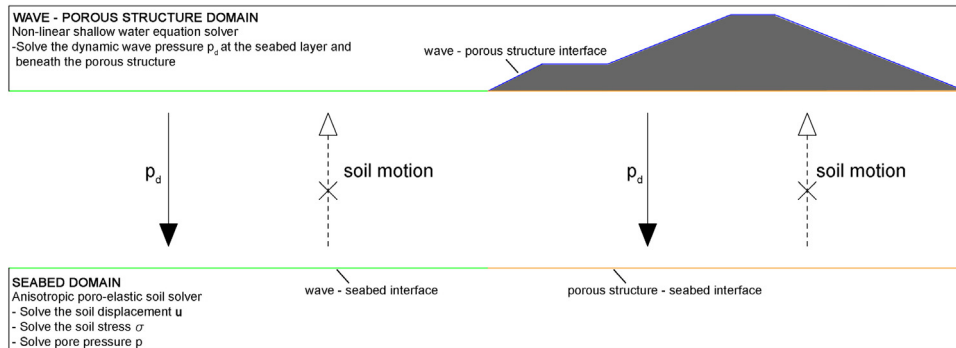


Fig. 1. One-way boundary coupling algorithm of wave-structure-seabed interaction.

are implemented at the interface, by interpolating the values from the supplied domain in space and time. Since the grid sizes and time steps for the two domains are allowed to be various, it increases the efficiency of solving the coupled system and allows the usage of different numerical tools.

### 3. Model verifications

The present numerical models have been validated in the previous studies. The SWASH model to simulate the interaction of submerged berms and the incident waves has been validated by Celli et al. [5], through a comparison with the experimental data (see their Figure 3). The poro-elastic soil model in OpenFOAM to simulate the wave-induced seabed response, has been validated by Li et al. [20], through a comparison with the experimental data provided by Tsai and Lee [36] (e.g. see their Figures 2,3 and 4). To further verify the numerical models for the present problems, grid convergence studies have been performed with SWASH and with the porous soil solver, respectively. In particular, the numerical model SWASH has been used to compute the wave-induced seabed pressure within the wave-porous structure interaction framework. At first, a series of preliminary tests have been carried out to evaluate the sensitivity of the results for different computational grid sizes. A rubble mound breakwater interacting with regular waves ( $H = 2$  m,  $T = 7$  s) has been simulated considering a domain length equal to 411 m and a series of computational grid spatial resolutions, ranging from 0.1 m up to 0.5 m. The water level and the seabed dynamic pressure time series have been collected at the same location for comparison purposes. Then zero-crossing analysis has been carried out and the mean values of the water wave heights and wave pressure heights have been evaluated. For a selected location (similar results are achieved for other points), Fig. 2 shows the normalized values of the water wave heights, i.e.  $H_{dx_i}/H_{dx0.1}$  (left panel) and the normalized values of the wave pressure heights i.e.  $P_{dx_i}/P_{dx0.1}$  (right panel), taking as a reference the results obtained for the finest grid resolution (i.e.  $H_{dx0.1}$  and  $P_{dx0.1}$ ).

With respect to the finest grid, it appears that the difference of the results computed by adopting  $dx = 0.2$  m is equal to 1.5% and 0.37% for the mean water wave heights and the mean wave pressure heights, respectively. Therefore, adopting a computational grid spatial resolution equal to 0.2 m suffices to achieve reliable numerical accuracy.

A grid convergence study has been carried out also for the soil model, simulating a 30 m thick and 450 m long portion of soil (Fig. 3), subjected to wave-induced seabed pressure acting on the upper boundary, adopting three different set of meshes (see Table 1). The dynamic pore pressures, collected in the sample point (see Fig. 3), have been compared as shown in Fig. 4.

It appears that as the number of grid points increases, the pore pressure converges to a higher amplitude (in absolute value). This implies that an insufficient number of points may underestimate the pore pressure in the seabed. As illustrated in Table 1, the relative change of minimum pressure derived from the finest tested mesh (Mesh No.3) and

the medium tested mesh (Mesh No.2) is 0.45%. Then,  $2.7 \times 10^5$  grid points (i.e. Mesh No.2) have been used to perform the parametric study described herein.

### 4. Numerical investigations

Momentary liquefaction occurs in very dense elastic seabed foundation and it is unlikely able to produce the total collapse of structures, if any. This does not mean the absence of potential serious damage that could be suffered by structures. Indeed, the momentary liquefaction can enhance the scouring process in front of rubble mound breakwaters, causing the partial failure of the armor layer. The damage could even reach the core, if a bedding layer is not used. The deployment of submerged berms could be hence very positive for the structure stability, since they are able to reduce the momentary liquefaction occurrences and the scouring process as well.

Therefore, the aim of this paper is to evaluate the performances of submerged berms in reducing the momentary liquefaction depths around and beneath a rubble mound breakwater. The results have been compared to those associated with the presence of a straight sloped conventional breakwater without a berm. In both cases, the absence of a transition layer beneath the armour layer and the berm is assumed by considering the rocks in direct contact with the seabed, loading the soil in a discontinuous way. It should be emphasized that various experimental (e.g. Kudella et al. [18]) and numerical (e.g. Ye et al. [42]) studies indicated the absence of momentary liquefaction occurrences underneath the breakwater, where the overburdened pressure is significantly enhanced by the self-gravity of the structure. In the work presented herein, all the momentary liquefaction occurrences appearing under the breakwaters are due to the discontinuous load acting on the soil, aimed to describe the absence of a transition layer under the berm. Therefore, under the assumption of bedding layer absence, the berm rocks load is transferred to the soil only in correspondence of the contact area (see Fig. 5). In the former zone, the vertical effective stresses, increased due to the weight of the rocks, decrease the liquefaction probability. On the other hand, the presence of unloaded areas (i.e. zones among two contiguous rocks) makes the soil potentially prone to momentary liquefaction occurrences. The former assumptions find justification if a safe rationale is employed.

Then, a parametric study has been carried out by varying the berm configuration (i.e. its length,  $L_b$ , and the water depth over the berm,  $h_b$ , see Fig. 6), keeping constant the offshore regular wave condition, the water depth and the elastic properties of the soil (see Table 2). A series of preliminary tests have been carried out to evaluate the sensitivity of dynamic seabed pressure to the armor layer porosity parameter variation. It was observed that a higher porosity of the armor layer leads to a higher amplitude of dynamic pressure on the underneath seabed. According to US Army Corps of Engineers (USACE) [38] and CIRIA/CUR/CETMEF [7], typical values of rock armor layer porosity are at most equal to 0.4. Therefore,  $n = 0.4$  is selected for modeling the berm and the armor layer in the present study. The value of the ratio  $h_b/h_t$  (being

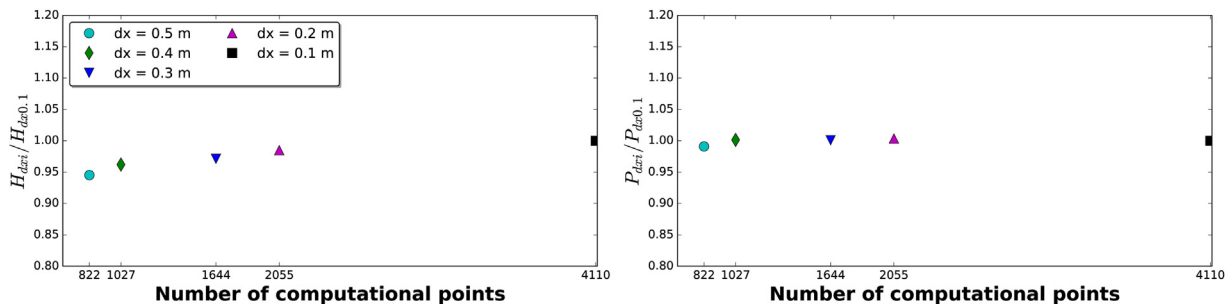
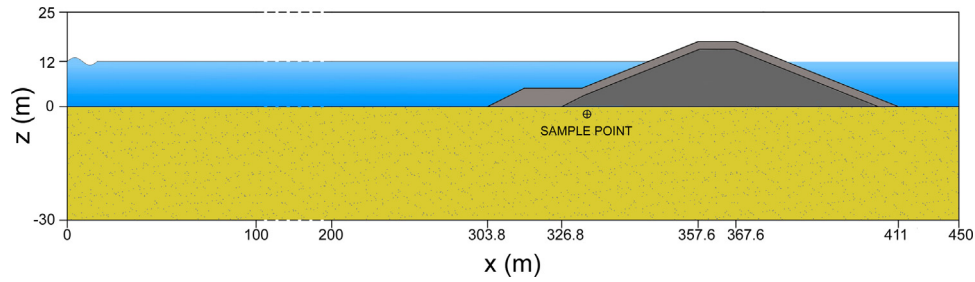


Fig. 2. Variation of the normalized water wave height  $H_{dx_i}/H_{dx0.1}$  (left panel) and of the normalized wave pressure height  $P_{dx_i}/P_{dx0.1}$  (right panel), as a function of the numbers of computational points of the mesh.





**Fig. 3.** Sketch of the computational domain implemented for the soil model convergence study. It is shown the sample point ( $x = 330.2$  m,  $z = -2$  m), where the pore pressures are collected.

**Table 1**

Mesh parameters for the soil model convergence study (relative change is evaluated with respect to the finest Mesh No.3).

Mesh	Number of grid points	Minimum pressure (Pa)	Relative change
No.1	$8.43 \times 10^4$	-5116.88	1.28%
No.2	$2.70 \times 10^5$	-5183.30	0.45%
No.3	$6.75 \times 10^5$	-5206.84	

$h_t$  the water depth at the toe of the berm) ranges from 0.2 up to 0.8, whilst the ratio  $L_b/L_w$  (being  $L_w$  the wave length at the toe of the berm) ranges from 0.040 up to 0.356 for a total of 62 simulations.

With the aim to evaluate the wave-induced seabed pressure for different submerged berm configurations (i.e. by varying the berm length  $L_b$  and the water depth over the berm  $h_b$ ), the simulations have been carried out by using SWASH numerical model, validated as described in the previous section.

Fig. 6 shows one of the used computational domain. As for the simulations carried out for the calibration of the model, the total length of the computational domain is set at 411 m and the cell size in the  $x$ -direction at 0.2 m. The model is run with three layers in the vertical direction, in order to properly describe the wave frequency dispersion. The offshore boundary is considered as weakly reflective and a water level time series, reproducing regular waves (see Table 2), is imposed. For each test case, almost 90 waves have been simulated. At the onshore boundary, the Sommerfeld radiation condition is applied.

For each tested berm configuration, the computed seabed dynamic pressure time series have been collected and used as coupling boundary condition for the anisotropic Biot's porous soil model.

The numerical domain of the porous seabed is 450 m long and 30 m thick. In order to avoid unwanted lateral boundary effects, a preliminary sensitivity study to evaluate the best structure location, inside the computational domain, has been carried out. Therefore, it has been decided to place the porous structure at a distance equal to almost  $4L_w$  from the left side of the computational domain (where  $L_w$  is the wave length at the toe of the berm, equal to 75.83 m). Moreover, the soil domain was extended of a quantity equal to 39 m starting from the breakwater end, in order to further limit the effect of the onshore

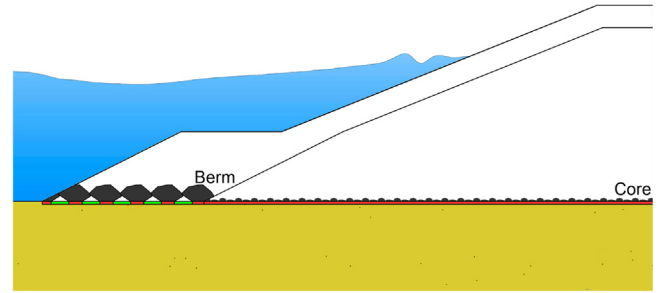


**Fig. 5.** Sketch of assumed load distribution under a porous structure: red zones refer to contact areas, where the load is transferred to the soil. Green zones refer to unloaded areas. (For interpretation of the references to color in this figure legend, the reader is referred to the web version of this article.)

boundary.

The properties of the seabed sand sediment are based on the measurements of the North sea soil by Kjekstad and Lunne [17], with reasonable assumptions concerning the anisotropic properties. Since the comparative nature of the present work, based on the evaluation of the submerged berms configuration effects on the momentary liquefaction occurrences, the importance of simulating several soil properties is not crucial. The soil porosity  $n$  is set 0.3 and the saturation factor  $S_r$  is set to 0.975. The anisotropic parameter settings are shown in Table 2. The boundary conditions of the seabed domain are specified as follows.

- (1) At the water-seabed and the porous structure-seabed interfaces (see Fig. 1), the effective soil stresses vanish, hence the soil has zero traction at the seabed surface. The pore pressure, at the aforementioned interfaces, is equal to the dynamic wave pressure acting on the seabed and beneath the porous structure.
- (2) At the bottom and lateral boundaries of the seabed, the soil skeleton is allowed to slip and the normal pore pressure gradient is zero.

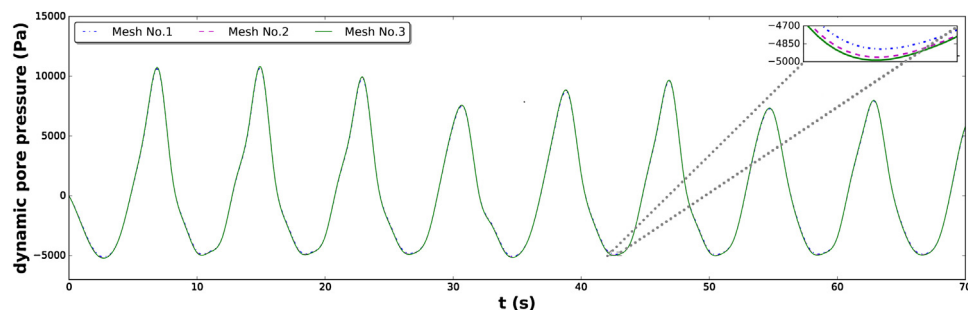


**Fig. 4.** Grid convergence for dynamic pore pressure in the seabed (sample point coordinates:  $x = 330.2$  m,  $z = -2$  m).

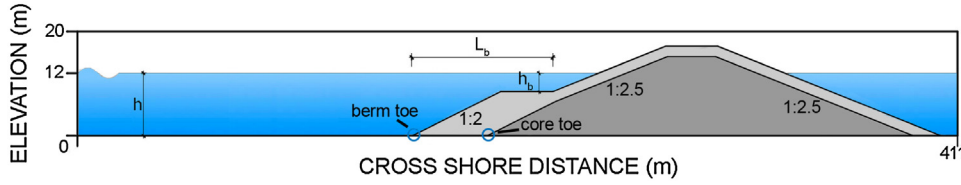


Fig. 6. Geometric parameters definition of conventional rubble mound breakwater with a berm. The berm and core toe positions could vary among the simulated test cases.

Table 2

Parameter settings for wave-structure-seabed interaction.

<i>Wave parameters</i>		
Wave height $H$ (m)	4.0	
Wave period $T$ (s)	8.0	
Water depth $h_t$ (m)	12.0	
Wave length $L_w$ (m)	75.8	
<i>Seabed parameters (directional values)</i>		
Young's modulus ( $N/m^2$ )	$E_x = 1.2 \times 10^7$	$E_z = 2.0 \times 10^7$
Poisson's ratios	$\nu_{xx} = 0.40$	
Shear modulus ( $N/m^2$ )	$G_{xx} = 5 \times 10^6$	
Permeability (m/s)	$k_x = 0.005$	$k_z = 0.001$

## 5. Results and discussion

### 5.1. Consolidation

The deployment of the breakwaters can significantly increase the effective stresses in the surrounding soil. Once the structure is built on the seabed, the self-weight of a breakwater is initially transferred to the pore water in the seabed foundation, resulting in the generation of excess pore pressure. Then, the soil will experience the gradual dissipation of the excess pore pressure. Consequently, the breakwater load is gradually transferred from the pore water to the soil skeleton. At the end of the process, the seabed foundation reaches an equilibrium consolidation status. Therefore, the determination of the initial consolidation status of seabed foundation under hydrostatic pressure and breakwater weight is an essential step in the evaluation of structures stability (Jeng and Ye [15]), since it is able to influence the potential probability of dynamic wave-induced soil liquefaction (e.g. Ulker et al.

[37], Sui et al. [32] and Zhao et al. [46]).

Fig. 7 (upper panel) shows the vertical soil displacement  $U_z$  after the completion of the consolidation process for the simulated test cases with  $h_b/h_t = 0.19$  and  $L_b/L_w = 0.35$ . A negative value of  $U_z$  indicates that the soil skeleton is compressed and moves downward. It appears that beneath the structure, the soil skeleton has been largely compressed compared to the far field. The vertical soil displacement under the berm is lower (in absolute value) than that under the breakwater core due to the berm reduced weight.

The lower panel of Fig. 7 shows the distribution of the vertical effective stresses  $\sigma'_z$  in the soil, at the end of the consolidation process. A negative value of  $\sigma'_z$  indicates the compression of the soil skeleton. It appears that the gravity of the structure is gradually transferred to the supporting soil skeleton. The portion of soil beneath the breakwater is characterized by higher (absolute) values of vertical effective stresses if compared to the far field. The lower panel of Fig. 7 also shows a compressive stress concentration at the berm-core interface as well as at the end of the breakwater. This effect is justified by the different gravitational load distributions between the submerged berm and the core, as well as between the loaded and unloaded areas at the end of the breakwater.

The vertical effective stresses  $\sigma'_z$  computed at the end of the consolidation process have been used as an initial condition for the momentary liquefaction analysis. It should be stressed that during the construction phase, when the consolidation state has not been reached, the vulnerability of the structure to liquefaction occurrences could be higher.

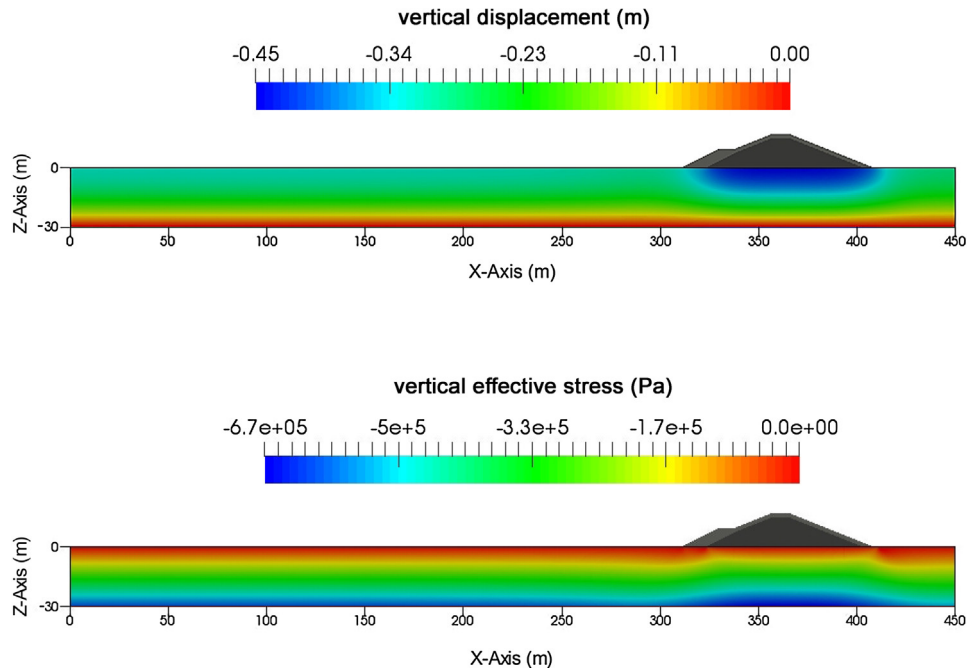
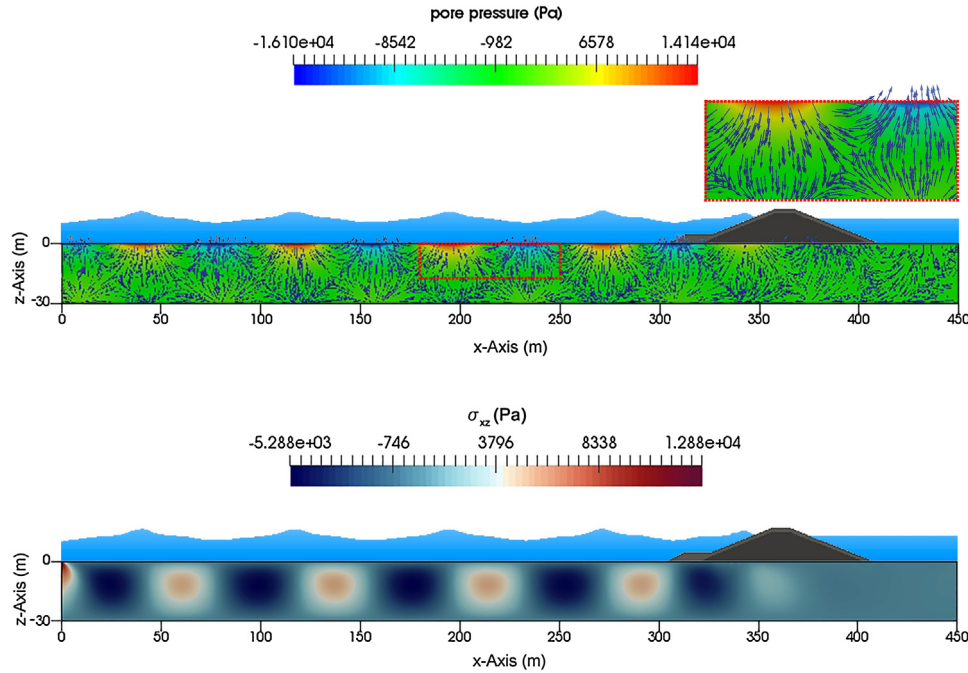


Fig. 7. Consolidation process results with reference to a breakwater with submerged berm characterized by  $h_b/h_t = 0.19$  and  $L_b/L_w = 0.35$ . Upper panel: vertical soil displacement  $U_z$  after the completion of the consolidation process. Lower panel: vertical effective stress  $\sigma'_z$  after the completion of the consolidation process.



**Fig. 8.** Wave-induced seabed response with reference to a breakwater with submerged berm characterized by  $h_b/h_t = 0.59$  and  $L_b/L_W = 0.3$ . Upper panel: transient pore pressure and seepage flow at the instant  $t = 676$  s ( $H = 4$  m). Lower panel: Shear stress  $\sigma_{xz}$  distribution in the seabed at the time instant  $t = 676$  s ( $H = 4$  m).

### 5.2. Wave-induced seabed response

Fig. 8 (upper panel) shows the wave-induced transient pore pressure and the seepage flow in the seabed at the time instant  $t = 676$  s, for one of the simulated test cases (i.e.  $h_b/h_t = 0.59$  and  $L_b/L_W = 0.3$ ).

As expected, the passage of wave crests induces positive transient pore pressures, whilst the transient pore pressures become negative under the wave troughs. The same big picture could be drawn focusing on the seepage flow. Its direction is directly related to the wave phases (e.g. Jeng et al. [16]). The seepage flow is directed downward during the passage of wave crests, leading to the compression of the soil. On the other hand, the seepage flow is directed upward during the passage of wave troughs, leading to the decompression of the soil. It should be underlined that the momentary liquefaction is directly related to the magnitude and direction of seepage forces. In particular, when the upward pore pressure gradient (strictly related to the seepage forces) exceeds the vertical initial effective stress, the momentary soil liquefaction is likely to occur and further affects the structure stability. The seabed does not liquefy when the seepage force is downward because it increases the contact effective stresses of soil particles (Jeng et al. [16]). More discussion about the liquefaction analysis is presented in the next section.

Fig. 8 (lower panel) shows the wave-induced shear stresses  $\sigma_{xz}$  in the seabed. By neglecting the seabed response close to the left boundary of the computational soil domain, affected by the lateral boundary proximity, it could be observed that under the periodic wave loading, the shear stresses  $\sigma_{xz}$  values switch from positive to negative periodically. In the present work, the shear failure is not investigated. Nevertheless, it should be stressed that the wave-induced cyclic dynamic shear stresses could be a crucial factor for the stability of breakwaters (Ye et al. [43]). They can lead to the progressive buildup pore pressure that may eventually be large enough to result in significant deformation of the soil (Nataraja and Gill [26]).

### 5.3. Momentary liquefaction analysis

The liquefaction criterion adopted in the present work is a modified version from Zen and Yamazaki [45]. The authors proposed a 1D

liquefaction criterion based on the excess pore pressure:

$$p(z, t) - p(0, t) \geq -(\gamma_s - \gamma_w)z \quad (10)$$

afterwards extended by Jeng [14] to the 3D cases:

$$p(z, t) - p(0, t) \geq -\frac{1 + 2K_0}{3}(\gamma_s - \gamma_w)z \quad (11)$$

where  $p(z, t)$  is the pore pressure in the seabed,  $p(0, t)$  is the pore pressure at the seabed surface,  $\gamma_s$  and  $\gamma_w$  are the unit weight of soil and water respectively,  $K_0$  is the coefficient of lateral earth pressure. It should be stressed that Eq. (11) is only applicable in absence of any structure. As for this work, if rubble mound breakwaters are concerned, the adopted momentary liquefaction criterion reads as follows:

$$p(z, t) - p(0, t) \geq \sigma'_{z0} \quad (12)$$

where  $\sigma'_{z0}$  represents the initial vertical effective stress induced by the gravitational forces from the consolidation process. The present criterion was used in the works of Sui et al. [32], Zhao et al. [46] and Li et al. [20]. In order to investigate the effects of submerged berm deployment, the adopted rationale imposes a comparison among the aforementioned series of results deriving from the deployment of a rubble mound breakwater without a berm. Fig. 9 shows the liquefaction depth achieved in the presence of the rubble mound breakwater without the submerged berm.

As for the rubble mound breakwaters with submerged berms, the simulation considers the armor layer rocks in direct contact with the seabed. Their arrangement leads to the existence of loaded areas (i.e. just beneath the rocks) and unloaded areas (i.e. zones between two contiguous rocks). Therefore, the rocks load is transferred to the soil only in correspondence of the contact area (see Fig. 5). In the former zone, the vertical effective stresses, increased due to the weight of the rocks, decrease the liquefaction probability. On the other hand, the presence of unloaded areas leads to a higher possibility of soil liquefaction compared to the loaded zones. The upper panel of Fig. 9 shows the maximum values of liquefaction depth around and beneath the structure, whereas in the lower panel, the maximum liquefied area has been divided into two subareas: the internal subarea (i.e. light green zone) shows what happens beneath the structure, whilst the external

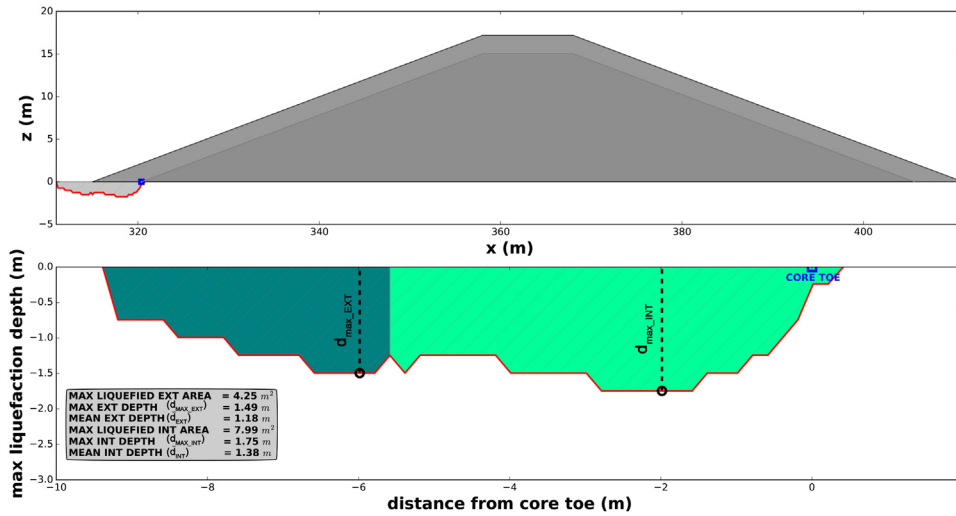


**Fig. 9.** Wave-induced momentary liquefaction with reference to a breakwater without submerged berm. Upper panel: momentary liquefaction maximum depth around and beneath the structure. Lower panel: zoom of the momentary liquefaction maximum area splits in two subareas, according to the location of the liquefaction occurrences. Dark green subarea refers to maximum liquefaction depth in front of the structure up to the breakwater toe. Light green subarea refers to maximum liquefaction depth beneath the structure. (For interpretation of the references to color in this figure legend, the reader is referred to the web version of this article.)

one (i.e. dark green zone) shows what happens in front of the structure, up to the breakwater toe. In the lower panel of Fig. 9, the origin of the coordinate system is located at the core toe. For each of the detected subareas, the maximum and the mean local depth (i.e. obtained dividing the subarea value by its superficial length) have been evaluated. From the inspection of Fig. 9 it appears that the maximum internal liquefaction depth (hereinafter referred to as  $d_{\max, \text{int}}$ ), equal to 1.75 m, is greater than the external one (hereinafter referred to as  $d_{\max, \text{ext}}$ ) equal to 1.49 m. Also the comparison among the mean maximum values (hereinafter referred to as  $\bar{d}_{\text{ext}}$  and  $\bar{d}_{\text{int}}$ ) confirms that in a rubble mound breakwater without submerged berm, the most exposed part to the momentary liquefaction occurrences is the area beneath the armor layer. Hence, the probability of the structure damage triggering is high in that location.

For the comparison purpose, Fig. 10 shows the maximum liquefaction depths in presence of a rubble mound breakwater with two different submerged berms characterized by  $h_b/h_t = 0.59$ ,  $L_b/L_w = 0.17$

(left panels) and  $h_b/h_t = 0.59$ ,  $L_b/L_w = 0.30$  (right panels), respectively.

The inspection of Fig. 10 reveals the positive effects of submerged berms deployment on the reduction of momentary liquefaction depth. From the comparison between the left panels of Fig. 9 and 10, it appears that even though  $d_{\max, \text{int}}$  remains the same,  $\bar{d}_{\text{int}}$  decreases down to 1.16 m, less than what is achieved in absence of berm (i.e. 1.38 m). Similar consideration applies for  $\bar{d}_{\text{ext}}$  that drops down to 0.54 m. The big picture description further improves looking at the right panels of Fig. 10. The deployment of a longer submerged berm implies a reduction of  $d_{\max, \text{int}}$  that drops down to 1.24 m as well as  $\bar{d}_{\text{int}}$  that is equal to 0.64 m. In contrast,  $d_{\max, \text{ext}}$  and  $\bar{d}_{\text{ext}}$  grow up reaching values equal to 0.99 m and 0.77 m, respectively. The latter phenomenon is likely due to the upward wave-induced pore pressure gradient rather than to a reduced initial vertical stress distribution, in view of the increased distance from the breakwater core. It should be emphasized that the behavior of maximum liquefaction depths under the porous structures is not smooth, as observable in the right panel of Fig. 10. This is due to the

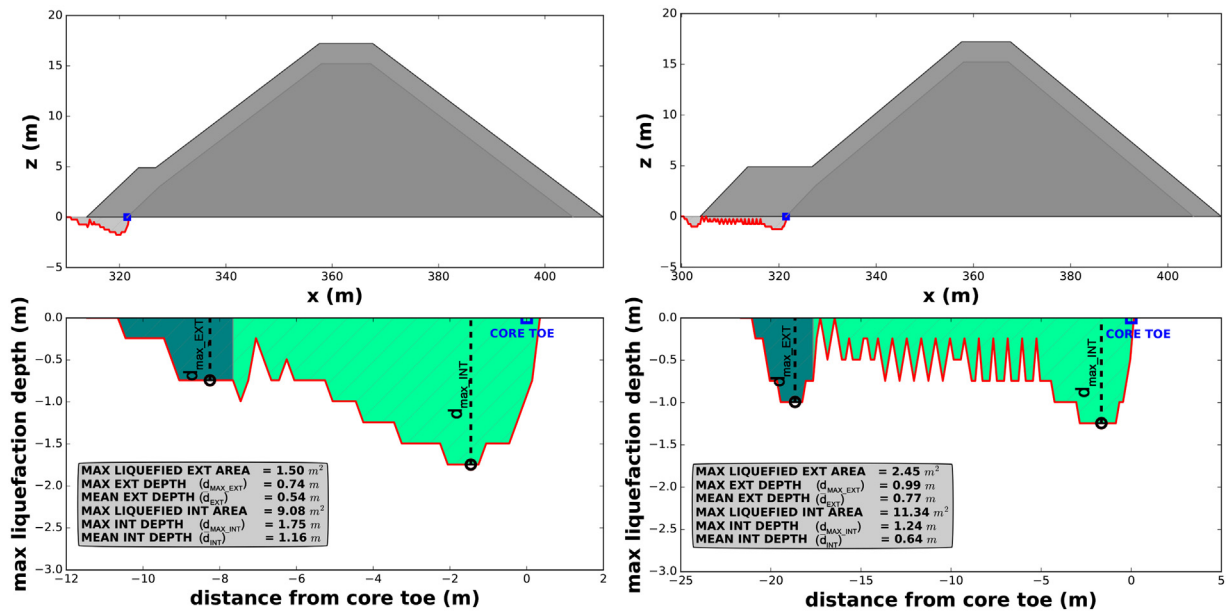


**Fig. 10.** Wave-induced momentary liquefaction with reference to breakwaters with submerged berms characterized by  $h_b/h_t = 0.59$  and  $L_b/L_w = 0.17$  (left panels),  $L_b/L_w = 0.30$  (right panels). Upper panels: momentary liquefaction maximum depth around and beneath the structure. Lower panels: zoom of the momentary liquefaction maximum area splits in two subareas, according to the location of the liquefaction occurrences. Dark green subareas refers to maximum liquefaction depth in front of the structure, up to the breakwater toe. Light green subareas refers to maximum liquefaction depth beneath the structure. (For interpretation of the references to color in this figure legend, the reader is referred to the web version of this article.)



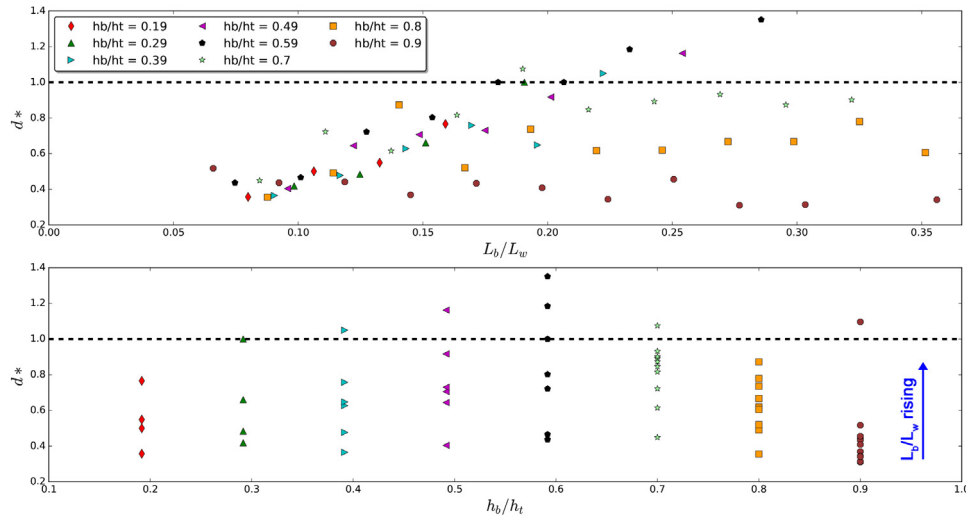


**Fig. 11.** Variation of  $d^*$ , (i.e. the ratio  $\bar{d}_{ext}/\bar{d}_{int}$ ) as a function of the dimensionless berm length ( $L_b/L_w$ , upper panel) and of the dimensionless water depth over the berm ( $h_b/h_t$ , lower panel).

rocks arrangement aimed to simulate the absence of the transition layer under both the berm and the armor layer. Looking again at Fig. 9, it appears that the maximum liquefied area for the straight sloped rubble mound breakwater is lower if compared to the liquefied areas of Fig. 10 where submerged berms are employed. Of course this is expected, since the contact length among the seabed and the structure increases as the berm length increases. However, this does not imply a growth of potential structure failure.

Basically, the longer the berm, the lower the momentary liquefaction probability near the breakwater core, and the higher the momentary liquefaction probability at the toe of the berm, where the stability of the armor layer is not compromised. The submerged berm could be hence intended as the expendable part of the structure. This concept could be better caught looking at the upper panel of Fig. 11, where  $d^*$  represents the ratio of  $\bar{d}_{ext}$  to  $\bar{d}_{int}$ , as a function of the dimensionless berm length  $L_b/L_w$ . Except for the lowest berms (i.e. characterized by  $h_b/h_t = 0.9$ ), the lengthening of the berm tends to push away the liquefaction probability from the zone beneath the breakwater to the area in front of the structure. Just for instance, the longest berms characterized by the ratio  $h_b/h_t$  equal to 0.49 and 0.59, lead to  $d^* > 1$ , i.e.  $\bar{d}_{ext} > \bar{d}_{int}$ . Nevertheless, the positive effects of the berm lengthening do not apply for the lowest berms, for which  $d^*$  remains almost constant varying the berm length. The inspection of the lower panel of Fig. 11 confirms that within the framework of long berms (i.e. roughly  $L_b/L_w \geq 0.20$ ), the best performances belong to those marked by  $h_b/h_t$  equal to 0.49 and 0.59. For short berms, roughly marked  $L_b/L_w \leq 0.1$ ,  $d^*$  is almost constant for different dimensionless water depth over the berm  $h_b/h_t$  values, i.e. a variation of the berm height does not induce appreciable modification on the area where liquefaction phenomena are likely to occur.

By focusing on the general behavior of submerged berms in influencing the liquefaction phenomena, the evaluation of the mean maximum liquefaction depth  $d_m$ , computed considering the whole liquefied area, could be helpful. By taking the mean maximum liquefied depth ( $d_{m0}$ ), achieved in presence of a straight sloped conventional breakwater without a berm as reference, Fig. 12 shows the variation of the ratio  $d_m/d_{m0}$  as a function of the dimensionless berm length  $L_b/L_w$  (upper panel) and of the dimensionless water depth over the berm  $h_b/h_t$  (lower panel).

In particular, from the inspection of the upper panel of Fig. 12 it is confirmed that, for the same water depth over the berm, the longer the berms, the higher the reduction of liquefaction depths around and beneath the structure. It has to be emphasized that even though high berms (i.e. characterized by lower values of  $h_b/h_t$ ) strongly affect the

wave propagation (e.g. Celli et al. [5]), the strongest influence on the momentary liquefaction occurrence belongs again to the berms characterized by the ratio  $h_b/h_t = 0.59$ . Higher berms tend to better attenuate the wave-induced pore pressure at the seabed interface, however, being heavier than the low ones, they enhance a stronger initial vertical effective stress reduction in the unloaded areas, i.e. where the armour elements are not in direct contact with the seabed. On the other hand, low berms (i.e. characterized by the ratio  $h_b/h_t$  ranging from 0.7 up to 0.9), being lighter than the high ones, marginally influence the initial vertical effective stress reduction, while at the same time, have no significant effect on the attenuation of the wave-induced pore pressure at the seabed interface. The influence of low berms length on momentary liquefaction attenuation is therefore negligible, being the ratio  $d_m/d_{m0}$  almost constant varying the ratio  $L_b/L_w$ .

The long berms, characterized by the ratio  $h_b/h_t = 0.59$ , could be hence intended as the right balance in terms of seabed pore pressure attenuation and initial vertical effective stress reduction. Therefore, within the range of the tested configurations, they could be regarded as the best design choice to limit the liquefaction phenomena. On a final note, the lower panel of Fig. 12 confirms that for short berms with a given length, the change of the berm height has no significant influence on the liquefaction occurrences, being the ratio  $d_m/d_{m0}$  almost constant varying the ratio  $h_b/h_t$ .

## 6. Concluding remarks

Berms deployed at the toe of conventional rubble mound breakwaters may be useful for various purposes, i.e. (i) to reduce wave loads acting on the breakwater armor elements, (ii) to reduce wave overtopping, (iii) to reduce momentary liquefaction occurrences under the structure, (iv) to protect from the scouring the breakwater toe. This research has numerically investigated the wave-induced soil response and the liquefaction probability around and beneath rubble mound breakwaters with submerged berm. Two numerical tools have been used for this study: the effects of submerged berms on the dynamic pressure acting on the seabed have been evaluated by means of SWASH, whereas the seabed responses to the wave-induced seabed pressures have been evaluated by using an ad-hoc anisotropic poro-elastic soil solver, developed in OpenFOAM (Li et al. [20]). A parametric study has been carried out by changing the berm configuration, to find out their performances in attenuating momentary liquefaction probability, especially under the breakwater core, where a partial failure could lead to a severe damage for the whole structure. For all the tested configurations, the effects of the consolidation process on the wave-induced

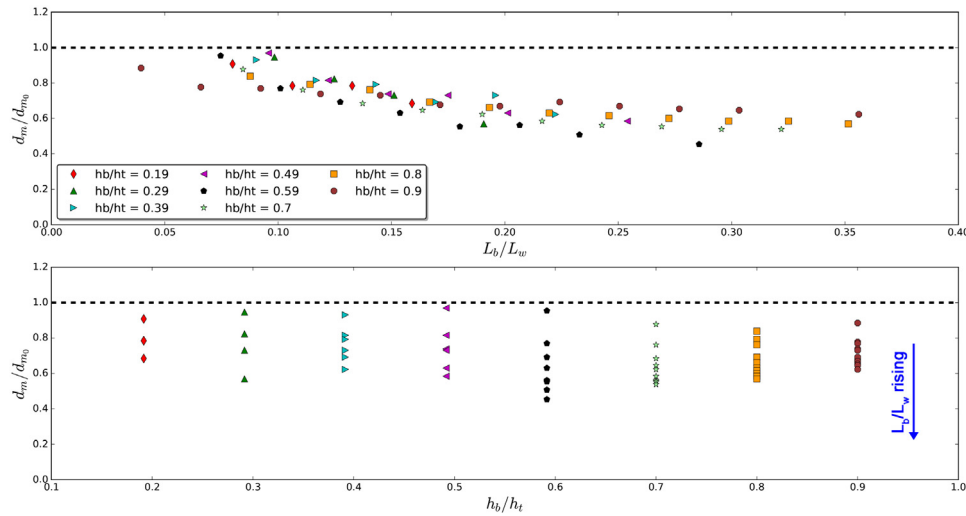


**Fig. 12.** Variation of the normalized mean maximum liquefaction depth  $d_m/d_{m0}$  as a function of the dimensionless berm length ( $L_b/L_w$ , upper panel) and of the dimensionless water depth over the berm ( $h_b/h_t$ , lower panel).

soil response, have been taken into account. Within the range of the tested configurations, the main conclusions are drawn as follows.

1. The presence of any berm tends to attenuate momentary liquefaction occurrences if compared to the case of a straight sloped conventional breakwater without a berm.
2. Except for the lowest tested berm (i.e. characterized by  $h_b/h_t = 0.9$ ), the lengthening of the berm tends to move the location where liquefaction probability is high, from the zone beneath the breakwater to the area in front of the structure, i.e. where a potential damage is less dangerous. Then, the main role of submerged berms is to protect the armor layer from momentary liquefaction occurrences and scouring process consequently. Basically, they could be intended as the expendable part of the structure.
3. High berms tend to better attenuate the wave-induced pore pressure at the seabed interface, however, being heavier than the low ones, they enhance a stronger initial vertical effective stress reduction in the unloaded areas. Consequently, the momentary liquefaction attenuation is limited.
4. Low berms, being lighter than the high ones, slightly influence the initial vertical effective stress reduction, while at the same time, have no significant effects on the attenuation of the wave-induced pore pressure at the seabed interface. The resulting momentary liquefaction attenuation is limited.
5. The greater momentary liquefaction attenuation is given by long berms characterized by the ratio  $h_b/h_t = 0.59$ , i.e. an intermediate height within the considered range, at least for the tested wave condition. They could be intended as the right balance in terms of seabed pore pressure attenuation and initial vertical effective stress reduction. Therefore, they could be regarded as the optimal design choice to prevent the liquefaction phenomena, within the tested conditions.

The present work has been carried out in a regular wave condition. More parametric studies on irregular waves will be covered in the future works.

## Acknowledgment

This study was supported in part with computational resources provided by the Norwegian Metacenter for Computational Science (NOTUR), under the project No: NN9372K.

## References

- [1] J. Alabart, A. Sanchez-Arcilla, G.P. Van Vledder, Analysis of the performance of swash in harbour domains, Proceedings of the 3rd IAHR Europe congress, 1–10. (2014), Porto, Portugal. IHAR, 2014.
- [2] M.A. Biot, General theory of three-dimensional consolidation, J. Appl. Phys. 12 (1941) 155–164.
- [3] J. Van den Bos, H.J. Verhagen, C. Kuiper, Numerical modelling of wave reflection and transmission in vertical porous structures, Proceedings 7th Coastal Structures conference (ASCE-COPRI), Boston, USA 9–11 September 2015 (authors version). ASCE-COPRI, 2015.
- [4] J. van den Bos, H.J. Verhagen, M. Zijlema, B. Mellink, Towards a practical application of numerical models to predict wave-structure interaction: an initial validation, Coast. Eng. Proc. 1 (2014) 50.
- [5] D. Celli, D. Pasquali, P. De Girolamo, M. Di Risio, Effects of submerged berms on the stability of conventional rubble mound breakwaters, Coast. Eng. 136 (2018) 16–25.
- [6] S. Chung, S. Kim, Y. Kang, J. Im, K. Nagendra Prasad, Failure of a breakwater founded on a thick normally consolidated clay layer, Geotechnique 56 (2006) 393–409.
- [7] CIRIA/CUR/CETMEF, The Rock Manual: The Use of Rock in Hydraulic Engineering Volume 683, (2007) Ciria.
- [8] M. Di Risio, I. Lisi, G. Beltrami, P. De Girolamo, Physical modeling of the cross-shore short-term evolution of protected and unprotected beach nourishments, Ocean Eng. 37 (2010) 777–789.
- [9] H. Elsafti, H. Oumeraci, A numerical hydro-geotechnical model for marine gravity structures, Comput. Geotech. 79 (2016) 105–129.
- [10] H. Elsafti, H. Oumeraci, Analysis and classification of stepwise failure of monolithic breakwaters, Coast. Eng. 121 (2017) 221–239.
- [11] L. Franco, Vertical breakwaters: the Italian experience, Coast. Eng. 22 (1994) 31–55.
- [12] J.R.C. Hsu, D.S. Jeng, Wave-induced soil response in an unsaturated anisotropic seabed of finite thickness, Int. J. Numer. Anal. Methods Geomech. 18 (1994) 785–807.
- [13] D.-S. Hur, C.-H. Kim, J.-S. Yoon, Numerical study on the interaction among a nonlinear wave, composite breakwater and sandy seabed, Coast. Eng. 57 (2010) 917–930.
- [14] D.-S. Jeng, Soil response in cross-anisotropic seabed due to standing waves, J. Geotech. Geoenviron. Eng. 123 (1997) 9–19.
- [15] D.-S. Jeng, J. Ye, Three-dimensional consolidation of a porous unsaturated seabed under rubble mound breakwater, Ocean Eng. 53 (2012) 48–59.
- [16] D.-S. Jeng, J.-H. Ye, J.-S. Zhang, P.-F. Liu, An integrated model for the wave-induced seabed response around marine structures: model verifications and applications, Coast. Eng. 72 (2013) 1–19.
- [17] O. Kjekstad, T. Lunne, Soil parameters used for design of gravity platforms in the north sea, Appl. Ocean Res. 3 (1981) 50–58.
- [18] M. Kudella, H. Oumeraci, M.B. de Groot, P. Meijers, Large-scale experiments on pore pressure generation underneath a caisson breakwater, J. Waterway Port Coast. Ocean Eng. 132 (2006) 310–324.
- [19] A. Lamberti, R. Archetti, M. Kramer, D. Paphitis, C. Mosso, M. Di Risio, European experience of low crested structures for coastal management, Coast. Eng. 52 (2005) 841–866 Low Crested Structures and the Environment.
- [20] Y. Li, M.C. Ong, T. Tang, Numerical analysis of wave-induced poro-elastic seabed response around a hexagonal gravity-based offshore foundation, Coast. Eng. 136 (2018) 81–95.
- [21] C. Liao, D. Tong, L. Chen, Pore pressure distribution and momentary liquefaction in vicinity of impermeable slope-type breakwater head, Appl. Ocean Res. 78 (2018)

- 290–306.
- [22] C. Liao, D. Tong, D.-S. Jeng, H. Zhao, Numerical study for wave-induced oscillatory pore pressures and liquefaction around impermeable slope breakwater heads, *Ocean Eng.* 157 (2018) 364–375.
  - [23] R. Marmoush, R. Mulligan, Physical Modelling and Non-Hydrostatic Numerical Modelling of Wave Propagation in a Wave Basin, (2016).
  - [24] H. Mase, T. Sakai, M. Sakamoto, Wave-induced porewater pressures and effective stresses around breakwater, *Ocean Eng.* 21 (1994) 361–379.
  - [25] H. Nago, S. Maeno, T. Matsumoto, Y. Hachiman, et al., Liquefaction and densification of loosely deposited sand bed under water pressure variation, The Third International Offshore and Polar Engineering Conference, International Society of Offshore and Polar Engineers, 1993.
  - [26] M. Nataraja, H. Gill, Ocean wave-induced liquefaction analysis, *J. Geotech. Eng.* 109 (1983) 573–590.
  - [27] H. Oumeraci, Review and analysis of vertical breakwater failures-lessons learned, *Coast. Eng.* 22 (1994) 3–29.
  - [28] D. Pasquali, M. Di Risio, P. De Girolamo, A simplified real time method to forecast semi-enclosed basins storm surge, *Estuar. Coast. Shelf Sci.* 165 (2015) 61–69.
  - [29] A. Saponieri, M. Di Risio, D. Pasquali, N. Valentini, F. Aristodemo, G. Tripepi, D. Celli, M. Streicher, L. Damiani, Beach profile evolution in front of storm seawalls: a physical and numerical study, *Coast. Eng. Proc.* 1 (2018) 70.
  - [30] A. Saponieri, N. Valentini, M. Di Risio, D. Pasquali, L. Damiani, Laboratory investigation on the evolution of a sandy beach nourishment protected by a mixed soft-hard system, *Water* 10 (2018).
  - [31] P. Smit, M. Zijlema, G. Stelling, Depth-induced wave breaking in a non-hydrostatic, near-shore wave model, *Coast. Eng.* 76 (2013) 1–16.
  - [32] T. Sui, J. Zheng, C. Zhang, D.-S. Jeng, J. Zhang, Y. Guo, R. He, Consolidation of unsaturated seabed around an inserted pile foundation and its effects on the wave-induced momentary liquefaction, *Ocean Eng.* 131 (2017) 308–321.
  - [33] B.M. Sumer, *Liquefaction Around Marine Structures*, World Scientific, 2014.
  - [34] T. Suzuki, C. Altomare, W. Veale, T. Verwaest, K. Trouw, P. Troch, M. Zijlema, Efficient and robust wave overtopping estimation for impermeable coastal structures in shallow foreshores using swash, *Coast. Eng.* 122 (2017) 108–123.
  - [35] The SWASH Team, *SWASH User Manual*, Version 4.01, (2017).
  - [36] C.-P. Tsai, T.-L. Lee, Standing wave induced pore pressures in a porous seabed, *Ocean Eng.* 22 (1995) 505–517.
  - [37] M. Ulker, M. Rahman, M. Guddati, Wave-induced dynamic response and instability of seabed around caisson breakwater, *Ocean Eng.* 37 (2010) 1522–1545.
  - [38] US Army Corps of Engineers (USACE), *Coastal Engineering Manual (CEM)*, USACE, Washington, DC, 2002.
  - [39] K. Vafai, C. Tien, Boundary and inertia effects on flow and heat transfer in porous media, *Int. J. Heat Mass Transf.* 24 (1981) 195–203.
  - [40] J.W. Van Der Meer, *Rock Slopes and Gravel Beaches Under Wave Attack*, (1988).
  - [41] M.R. Van Gent, Rock stability of rubble mound breakwaters with a berm, *Coast. Eng.* 78 (2013) 35–45.
  - [42] J. Ye, D. Jeng, R. Wang, C. Zhu, Numerical simulation of the wave-induced dynamic response of poro-elastoplastic seabed foundations and a composite breakwater, *Appl. Math. Model.* 39 (2015) 322–347.
  - [43] J. Ye, D.-S. Jeng, A. Chan, R. Wang, Q. Zhu, 3d integrated numerical model for fluid-structures-seabed interaction (FSSI): elastic dense seabed foundation, *Ocean Eng.* 115 (2016) 107–122.
  - [44] J. Ye, D.-S. Jeng, P.-F. Liu, A. Chan, W. Ren, Z. Changqi, Breaking wave-induced response of composite breakwater and liquefaction in seabed foundation, *Coast. Eng.* 85 (2014) 72–86.
  - [45] K. Zen, H. Yamazaki, Mechanism of wave-induced liquefaction and densification in seabed, *Soils Found.* 30 (1990) 90–104.
  - [46] H.-Y. Zhao, D.-S. Jeng, J. Zhang, C. Liao, H. Zhang, J. Zhu, Numerical study on loosely deposited foundation behavior around a composite breakwater subject to ocean wave impact, *Eng. Geol.* 227 (2017) 121–138 *New Advances in Coastal Engineering Geology and Geotechnics*.
  - [47] H.-Y. Zhao, Z. Liang, D.-S. Jeng, J. Zhu, Z. Guo, W. Chen, Numerical investigation of dynamic soil response around a submerged rubble mound breakwater, *Ocean Eng.* 156 (2018) 406–423.
  - [48] H.-Y. Zhao, D.-S. Jeng, Numerical study of wave-induced soil response in a sloping seabed in the vicinity of a breakwater, *Appl. Ocean Res.* 51 (2015) 204–221.
  - [49] M. Zijlema, G. Stelling, Efficient computation of surf zone waves using the nonlinear shallow water equations with non-hydrostatic pressure, *Coast. Eng.* 55 (2008) 780–790.
  - [50] M. Zijlema, G. Stelling, P. Smit, Swash: an operational public domain code for simulating wave fields and rapidly varied flows in coastal waters, *Coast. Eng.* 58 (2011) 992–1012.
  - [51] M. Zijlema, G.S. Stelling, Further experiences with computing non-hydrostatic free-surface flows involving water waves, *Int. J. Numer. Methods Fluids* 48 (2005) 169–197.